



## Highly durable 3D conductive matrixed silicon anode for lithium-ion batteries

Rasim Batmaz<sup>a,1</sup>, Fathy M. Hassan<sup>a,1</sup>, Drew Higgins<sup>b</sup>, Zachary P. Cano<sup>a</sup>, Xingcheng Xiao<sup>c</sup>, Zhongwei Chen<sup>a,\*</sup>

<sup>a</sup> Department of Chemical Engineering, Waterloo Institute for Nanotechnology, University of Waterloo, Waterloo, Ontario, N2L 3G1, Canada

<sup>b</sup> Department of Chemical Engineering, Stanford University, Stanford, CA, 94305, United States

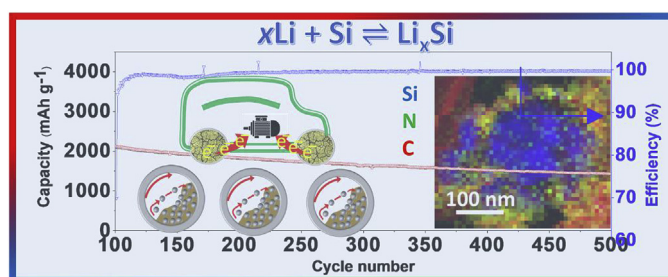
<sup>c</sup> Chemical Sciences and Materials Systems, General Motors Global Research and Development Center, Warren, MI, 48090, United States



### HIGHLIGHTS

- A highly durable micron silicon anode is proposed for lithium-ion batteries.
- A low-cost fluid induced fracture used to downsize the silicon microparticles.
- Electrode level thermolysis is applied to tune the structure of the electrode.
- The engineered electrode structure alleviated volume change of silicon particles.
- The electrodes exhibited high battery performance.

### GRAPHICAL ABSTRACT



### ARTICLE INFO

#### Keywords:

Lithium-ion battery  
Silicon  
Energy storage  
Polyacrylonitrile  
Fluid induced fracture

### ABSTRACT

Silicon is a strong candidate for next generation Li-ion batteries due to its high lithium storage capacity. However, to overcome electrode degradation caused by large volumetric changes during battery cycling, prohibitively expensive nanoscale synthesis techniques are typically required. To address this challenge, a low-cost methodology using fluid-induced fracture (FIF) is developed for accelerated nanoscaling of commercial micron-sized silicon and an electrode level thermolysis process is applied for the cyclization of polyacrylonitrile (cPAN) binder to form a 3D conductive anode matrix with micro-channels. This engineered matrix sandwiches the silicon particles leading to an electrode structure with incredible mechanical robustness which can accommodate the large volumetric changes occurring during battery charging and discharging. Thus, it can deliver an excellent capacity of 3081 mAh g<sup>-1</sup> at 0.1 A g<sup>-1</sup> and good cycle life (1423 mAh g<sup>-1</sup> @ 2 A g<sup>-1</sup> after 500 cycles). Furthermore, the simplicity and scalability of this approach provides a promising path forward for the commercialization of next generation Li-ion batteries based on high capacity silicon anodes.

### 1. Introduction

Lithium-ion (Li-ion) batteries are a ubiquitous rechargeable battery technology that dominates the portable electronics market. However, their limited energy density does not meet the requirements of long-

range electric vehicles and long-duration grid-scale energy storage systems [1]. In the past decade, intense efforts have focused on the development of next generation positive and negative electrodes to increase the storage capacity of Li-ion batteries. For the negative electrode, silicon has attracted significant attention due to its high lithium

\* Corresponding author.

E-mail address: [zhwchen@uwaterloo.ca](mailto:zhwchen@uwaterloo.ca) (Z. Chen).

<sup>1</sup> These authors contributed equally.

storage capacity ( $\sim 4200 \text{ mAh g}^{-1}$ ), low discharge potential ( $\sim 0.5 \text{ V}$  versus  $\text{Li/Li}^+$ ), natural abundance and environmentally friendly properties [2,3]. However, the enormous volume changes of silicon particles during lithium insertion and extraction leads to pulverization of silicon particles. This results in loss of electrical contact within the electrode and formation of an unstable solid-electrolyte interface (SEI) on the silicon surface, ultimately manifesting in rapid capacity decay [4–6]. Since the pioneering work of Cui et al. [7] on silicon nanowires as anode active materials, silicon nanomaterials have been extensively used to address the aforementioned problems [6,8–13]. It was found that silicon is intrinsically resistant to particle fracturing below a critical size of 150 nm, with particles in this size regime helping to maintain the integrity of the electrode [14]. Furthermore, small particle sizes shorten the lithium-ion diffusion path lengths, leading to less polarization losses and enhanced rate performance. In the last several years, nano-architected silicon electrodes were fabricated to improve the stability of silicon-based anodes. This has involved the use of 0D silicon nanoparticles [8–12,15] and 1D silicon nanowires [13,16] and nanotubes [6]. Despite good cycling performance achieved with these unique electrode architectures, the commercialization of these electrodes is not yet feasible due to the processing complexity associated with nanostructuring of silicon materials, often requiring expensive and complex synthesis methods such as chemical vapor deposition or template growth. Therefore, the utilization of silicon microparticles (SiMPs) is more attractive due to their widespread availability and low cost.

In earlier studies, the durability of SiMPs suffered significantly from particle fracturing and detachment from the electrode surface upon deep discharging [17–19], leading to poor cycle life including a 20% capacity loss in just 10 cycles. The cycling stability limitation of SiMPs electrodes was circumvented by applying a cut-off voltage. This helped to maintain a two-phase (crystalline-amorphous) silicon microstructure in which only the amorphous phase is active [18]. However, controlling the discharge potential reduces the energy density of the electrode since the crystalline core of the particle remains inactive [18]. To address this problem, SiMPs were engineered by chemical etching with hydrofluoric acid to create internal void spaces in the electrode to buffer the volume change occurring with deep galvanostatic cycling [20–22], whereas exterior void spaces were created by encapsulating the SiMPs with graphene [23]. Despite promising achievements in cycling performance, the scalability of these electrode manufacturing processes is limited due to the hazardous nature of the etching techniques. Aside from chemical etching, ball milling of SiMPs with carbon materials has been extensively used to reduce the silicon particle size and enhance cycling performance [24–28]. However the cells prepared from these SiMPs-carbon composites suffered from electrode level fracturing [29], which resulted in low capacity and insufficient cycle life. This arose due to the mechanically rigorous nature of milling, which only provides a physical mixing of individual components, as opposed to forming an intimate and strategic electrode structure.

It is therefore a prudent approach to retool existing processing techniques to engineer desired electrode structures and enhance battery cycling. Heat treatments are a popular electrode fabrication technique to carbonize polymeric precursors around electrode active materials (i.e., silicon) to provide electronic connectivity throughout the entire 3D electrode structures. However, the volumetric changes during battery cycling commonly lead to rupturing of the electrode from the current collector, resulting in electronic conductivity losses and poor electrode utilization due to active material isolation. Heat treatment should therefore be tuned not only to help enhance electronic interconnectivity of the active materials, but also to induce void space formation that can provide mechanical stability during battery cycling.

Herein, we developed a two-stage top down approach to prepare core-shell structured silicon-carbon nano-composite electrodes using commercially available micron-sized silicon particles as precursors. In the first stage, a new fluid-induced fracture (FIF) technique was applied to a slurry consisting of SiMPs, sulfur-doped graphene (SG),

polyacrylonitrile (PAN) and dimethylformamide (DMF). This FIF process was carried out to reduce the size of SiMPs, after which the slurry was coated on a copper foil current collector. After drying, the electrodes were subjected to thermolysis to engineer the chemical structure of the binder and architecture of the electrode. The synergistic effect of FIF and thermolysis resulted in a hierarchically structured silicon anode in which broken down SiMPs were wrapped with cyclized PAN (cPAN) and SG sheets. This conductive matrix around the silicon particles provides high mechanical resiliency, helping to accommodate significant volume change, while enhancing the electronic conductivity of the electrodes through the intrinsic conductivity of delocalized electrons of cPAN and SG sheets. In addition, the cyclization of PAN induced the formation of micron-sized channels throughout the electrode structure. These void micro-channels acted as a mechanical buffer for the anisotropic volume changes of silicon particles during battery charging/discharging, thereby preventing electrode pulverization. This electrode architecture leads to superior performance compared with conventional electrodes. Therefore, the concept of FIF and thermolysis provides a new route for low-cost electrode preparation with excellent electrochemical performance. Furthermore, the fabrication approach developed herein provides an efficient and non-hazardous manufacturing process for SiMPs based anodes that can be deployed at scale.

## 2. Experimental

**Preparation of Graphene Oxide (GO):** The reaction procedure to prepare GO from natural graphite flakes was adapted from James Tour method [30]. A 9:1 mixture of concentrated  $\text{H}_2\text{SO}_4/\text{H}_3\text{PO}_4$  (360:40 ml) was poured into a beaker containing 3 g of graphite powder. The solution was mixed for 30 min in an ice bath and then 27 g of  $\text{KMnO}_4$  was added to the solution for 1 h. It was then transferred to a hotplate and stirred at  $50^\circ\text{C}$ . After the reaction was completed, 600 ml distilled water was added to the solution while the solution remained stirring in an ice bath. After the addition of water, 30 ml hydrogen peroxide ( $\text{H}_2\text{O}_2$ ) was poured into the solution to reduce the unreacted  $\text{KMnO}_4$ . The final solution was washed several times with 5% HCl solution and distilled water by centrifugation.

**Preparation of Sulfur Doped Graphene (SG):** 150 mg of as prepared GO and 150 mg of phenyl disulfide were grinded in a mortar to mix each other. The mixture was annealed at  $1000^\circ\text{C}$  for 30 min in argon atmosphere and cooled to room temperature.

**Electrode Fabrication and Coin Cell Assembly:** The electrodes have been fabricated via direct coating of slurry onto copper foil using the Dr. Blade method. The SG-SiMPs-PAN slurry was prepared by wet ball milling 55 wt% SiMPs, 22 wt% PAN, 22 wt% SG, and 1 wt% GO in presence of dimethylformamide (DMF). A conventional reference cell was fabricated similarly for comparison. After coating the slurry, it was dried in a convection oven at  $80^\circ\text{C}$  overnight. The foil was punched by a disc cutter to form circular working electrodes. The electrodes were subjected to thermolysis at  $450^\circ\text{C}$  in argon atmosphere. The heating ramp during annealing was  $7.5^\circ\text{C min}^{-1}$ .

Coin type half cells were assembled in a glove box under argon atmosphere where the oxygen and water moisture level were less than 0.5 ppm. The electrolyte was  $\text{LiPF}_6$  (1 M) dissolved in 60 wt% dimethyl carbonate (DMC), 30 wt% ethylene carbonate (EC), and 10 wt% fluorinated ethylene carbonate (FEC). Lithium metal was used as a counter electrode. The electrodes were separated by using a polypropylene separator (PP2075, Celgard). The battery performance was tested by galvanostatic charge/discharge cycling by using a battery testing instrument (BTS 3000, Neware, China) with cut off voltages being 0.01 V and 1.1 V for discharge and charge, respectively. Different current densities were applied to investigate the rate capability. Finally, the coin cells were scanned between 1.5 V and 0.01 V at a rate of  $0.05 \text{ mV s}^{-1}$  to perform cycling voltammetry by using an electrochemical testing platform (Princeton Applied Research, VersaSTAT MC Potentiostat).

A conventional/reference cell was fabricated using 60 wt% SiMPs, 20 wt% Super P and, 20 wt% polyvinylidene fluoride (PVDF) and was tested under the same conditions of the SG-SiMPs-cPAN cells.

**Material Characterization:** The morphology and the structure of the electrode materials were studied using scanning electron microscopy (SEM, LEO FESEM 1530) and transmission electron microscopy (TEM, JEOL, 2010F TEM/STEM field emission microscope) equipped with a large solid angle for high X-ray throughput, and a Gatan imaging filter (GIF) for energy filtered imaging. Thermal analysis of samples was conducted by differential scanning calorimetry (DSC) and thermogravimetric analysis (TGA) by using TA instrument Q500. PAN was heated under nitrogen atmosphere from 25 °C to 850 °C at a ramp rate of 10 °C min<sup>-1</sup>. Raman spectra of PAN film and electrodes were recorded using a Bruker Senterra with a laser wavelength of 532 nm. FTIR analysis was conducted by PerkinElmer-283 B FT-IR spectrometer. XRD analysis was done by using monochromatic Cu K x-rays (154 nm wavelength) and an Inel XRG 3000 diffractometer. Atomic force microscopy (AFM) measurements were conducted with a Bruker Innova AFM in tapping mode.

### 3. Results and discussion

The developed electrode preparation process is shown schematically in Fig. 1a. The FIF technique involved wet milling of SiMPs, SG and PAN in the presence of DMF to prepare the slurry. One hour of milling was sufficient to reduce the size of the silicon particles from the micro- to the nanoscale, compared to previous studies that employ milling times in the range of 4 h–150 h [24–28]. The presence of fluid during the milling process induces accelerated silicon microparticle fracture into nanoparticles, in a manner we consider similar to the accelerated break down of geological rock formations in the presence of a pressurized fluid [31–33]. Scanning electron microscopy (SEM) images (Fig. 1b–c) and corresponding statistical analyses (Fig. 1d–e) show that the size of the SiMPs reduced from ca. 3.0 μm to ca. 500 nm (Fig. 1f) after 1 h of FIF. Conversely, when SiMPs were dry-milled for 1 h in the absence of a fluid, the size reduced to only ca. 1.2 μm, demonstrating the important role the fluid plays in the size reduction of SiMPs (Fig. S1a–b). Furthermore, as shown in Fig. S1c–d, the broadening of the primary silicon (220) x-ray diffraction (XRD) peak reveals the reduction in crystallinity and average crystallite size of the SiMPs that underwent FIF. After slurry coating on a copper foil current collector, the thermolysis process was applied at 450 °C in an argon environment to

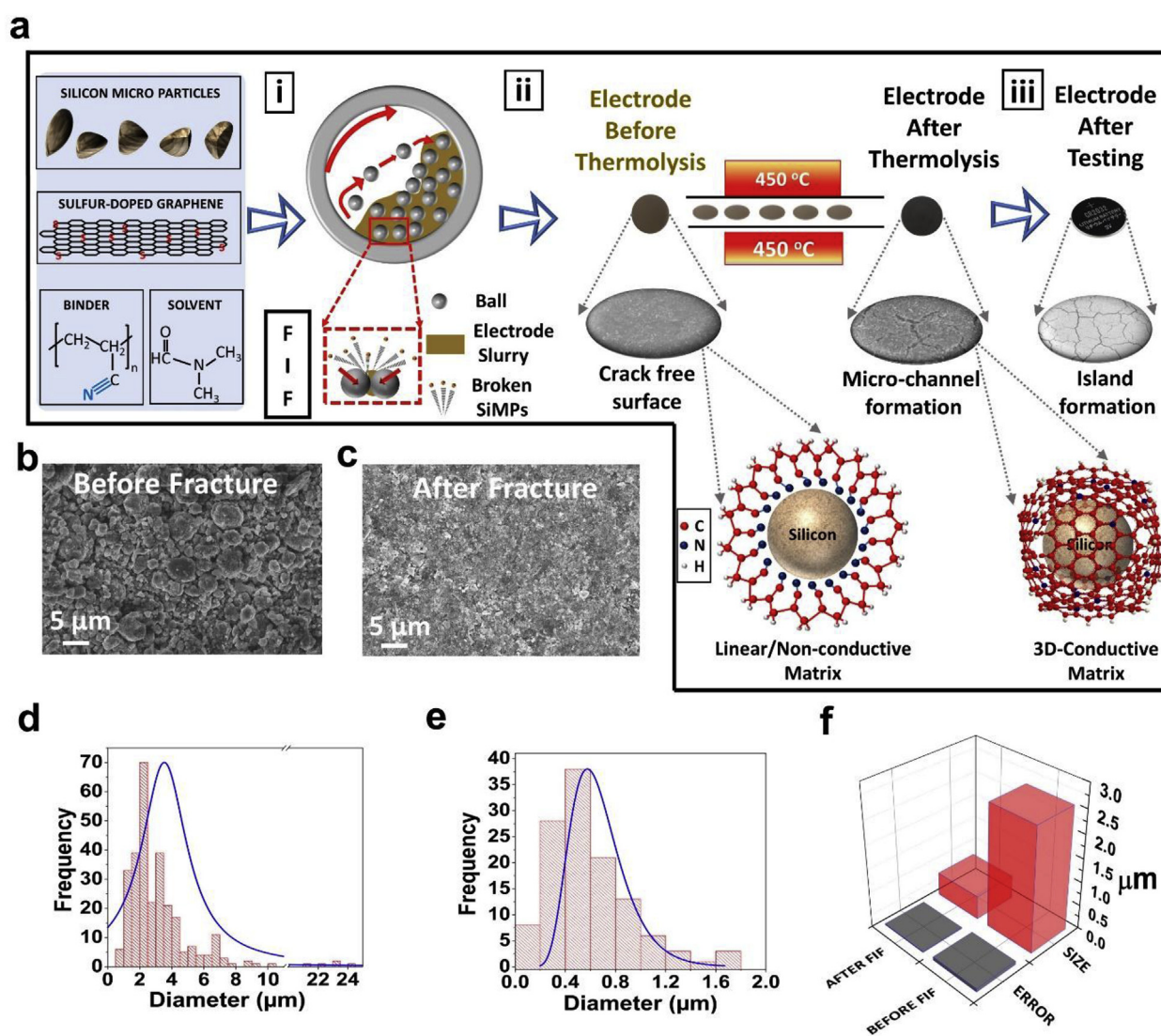


**Fig. 1.** (a) Schematic of the electrode fabrication process: (i) milling of the electrode slurry before coating; (ii) thermolysis of the electrodes; (iii) integration into coin cells for battery testing, (b) SEM image of SiMPs before FIF, (c) SEM image of electrode surface after FIF, (d) particle size distribution of SiMPs before FIF, (e) particle size distribution of SiMPs after FIF, (f) average particle size comparison of SiMPs before and after FIF.

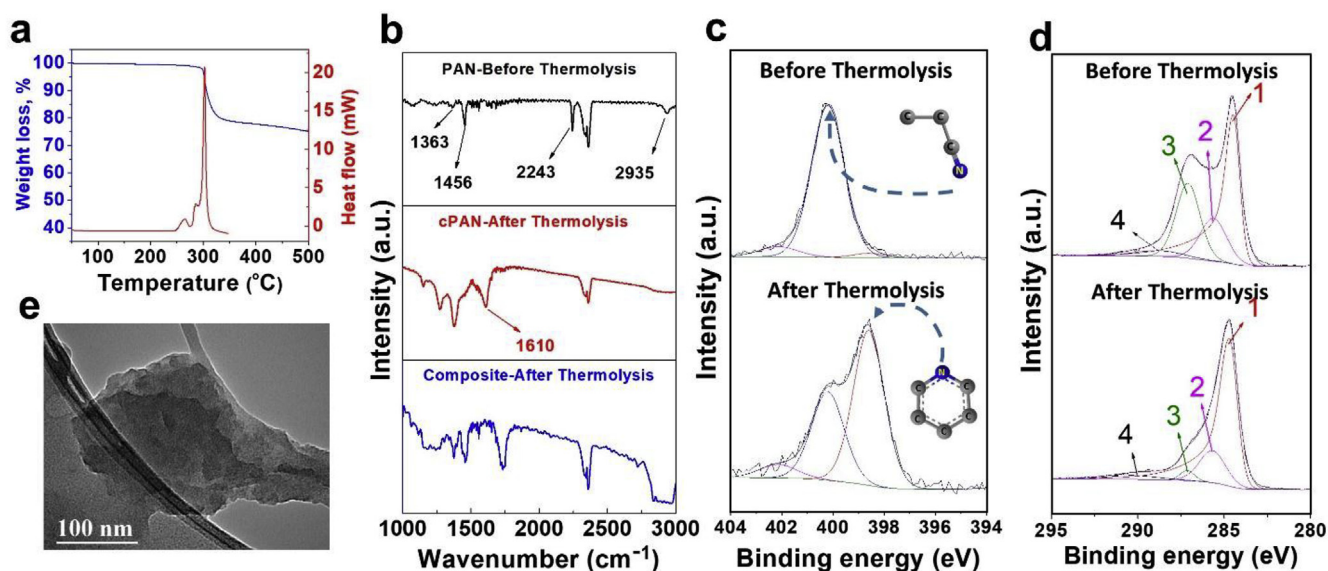


Fig. 2. (a) Thermal characterization of PAN by DSC and TGA, (b) FTIR spectra of PAN before and after thermolysis and SG-SiMPs-cPAN composite after thermolysis, (c) high resolution XPS spectra of nitrogen in SG-SiMPs-PAN composite before and after thermolysis, (d) high resolution XPS spectra of carbon in SG-SiMPs-PAN composite before and after thermolysis, (e) TEM image of cPAN after thermolysis.

engineer the electrode architecture. Upon thermolysis, no material rupture and deflagration were observed even after the electrodes were twisted and bended as seen in Figure S2, attributed to the mechanical resiliency of the cPAN.

Differential scanning calorimetry (DSC) was used to elucidate the thermal behavior of PAN. As shown in Fig. 2a, there is a sharp exothermic DSC peak around 300 °C, which was attributed to the cyclization of the polymer backbone (Figure S3a). Thermal gravimetric analysis (TGA) was also in good agreement with DSC. The mass loss was initiated at a similar temperature where the DSC peak appeared. In this region, 20% of the mass loss stemmed from the dehydrogenation of the polymer structure upon the formation of  $\pi$  conjugate bonds [34]. In addition to the thermal analysis, the chemical transformation of PAN was elucidated by Fourier transform infrared spectroscopy (FTIR) before and after thermolysis (Fig. 2b). Of particular interest was the cyanide group ( $C\equiv N$ ), as the absence/presence of this peak can be attributed to the cyclization of PAN. For pristine PAN, the peak at  $2243\text{ cm}^{-1}$  was assigned to the  $C\equiv N$  stretching, and the other peaks at  $1363$ ,  $1456$  and  $2935\text{ cm}^{-1}$  were characteristics of  $\delta_{C-H}$  in  $CH$ ,  $\delta_{C-H}$  in  $CH_2$  and  $\nu_{C-H}$  in  $CH_2$ , respectively (Fig. 2b) [35,36]. After applying thermolysis to PAN powder, the  $C\equiv N$  peak at  $2243\text{ cm}^{-1}$  disappeared, whereas a distinct peak appeared at  $1610\text{ cm}^{-1}$  which can be attributed to the  $C=C$  and  $C=N$  stretching [37] (Fig. 2b). This reveals that the PAN lost its linear chain structure and evolved to a graphite-like structure by a cyclization process (depicted schematically in Figure S3a). In addition, the disappearance of the  $C\equiv N$  peak at  $2243\text{ cm}^{-1}$  was also observed when the PAN was mixed with SiMPs and SG which shows that the cyclization of PAN also took place within the electrode material after thermolysis (Fig. 2b). This led to the formation of a robust 3D elastic and conductive network within the electrode, facilitating the charge transfer between the silicon particles, SG sheets and copper surface. Furthermore, FTIR spectra also provided insight into the possibility of interaction between the silicon atoms on the particle surface and cPAN after thermolysis. The peak at  $840\text{ cm}^{-1}$  was attributed to the asymmetric stretching mode of Si-N [38] (Figure S4). We believe that cPAN may bind with silicon atoms on the surface of the particles. This bond can help cPAN to strongly attach on the surface of silicon particles, thus stabilizing the electrode structure and preventing agglomeration which help to maintain the electrode integrity. Cyclization of PAN yields sheets-like morphology analogous to layered

nitrogen-doped graphene (NG). The TEM image in Fig. 2e clearly shows that the PAN cyclization after thermolysis forms sheet-like morphology which is believed to be multi-layered NG. Raman spectra of PAN and the electrodes clearly confirmed the formation of G-band and D-band after thermolysis (Figure S3). The structural evolution of the SG-SiMPs-PAN composite was further investigated by X-ray photoelectron spectroscopy (XPS) before and after thermolysis. Fig. 2c shows the N 1s spectra of the SG-SiMPs-PAN composite, which clearly confirmed the transformation of the nitrile group ( $C\equiv N$ ,  $400.1\text{ eV}$ ) to pyridinic nitrogen ( $398.6\text{ eV}$ ) after thermolysis [39,40]. In addition, the XPS spectra of C 1s reveals the enrichment of  $sp^2$  carbon after thermolysis, as shown in Fig. 2d. Further discussions about the electrode structure elucidation are included in the Supporting Information. The above discussion elucidating the electrode structure reveals that the electrodes subjected to thermolysis possessed multilayer architecture comprising SG, and NG resulting from cPAN. The silicon particles are nested and sandwiched between these multi-layered structures. The covalent interaction between the high electronegative atoms of N/S, and C/Si maintains the electrode stability by preventing agglomeration, in addition to strong adherence to the current collector [10]. The robust/strong nature of the layers of SG and the in-situ formed NG provide a strong and elastic skeleton that compensates volumetric changes during charge/discharge.

The electrode morphology and structure were investigated by high-angle annular dark field scanning transmission electron microscopy (HAADF-STEM). In this imaging mode, the regions of silicon particles appear brighter compared to the regions of the carbon matrix. The HAADF-STEM image (Fig. 3a) and corresponding energy dispersive spectroscopy (EDS) mapping (Fig. 3b–e) clearly shows that the silicon particles were embedded in the carbon matrix after thermolysis. To focus more on the surface of silicon particles, electron energy-loss spectroscopy (EELS) mapping was conducted at the selected region ( $Si_1$ ). As shown by Fig. 3f–k, silicon atoms are surrounded by carbon (C), nitrogen (N), oxygen (O) and sulfur (S) atoms. This further confirms that the silicon particles are wrapped by the carbon matrix of NG and SG, which are the only sources for C, S, N and O atoms. Thus, this illustrates that the cyclization of PAN took place at the surface of silicon particles which helped to form a robust electrode structure with high mechanical resiliency and conductivity.

The electrochemical performance of the fabricated SG-SiMPs-cPAN

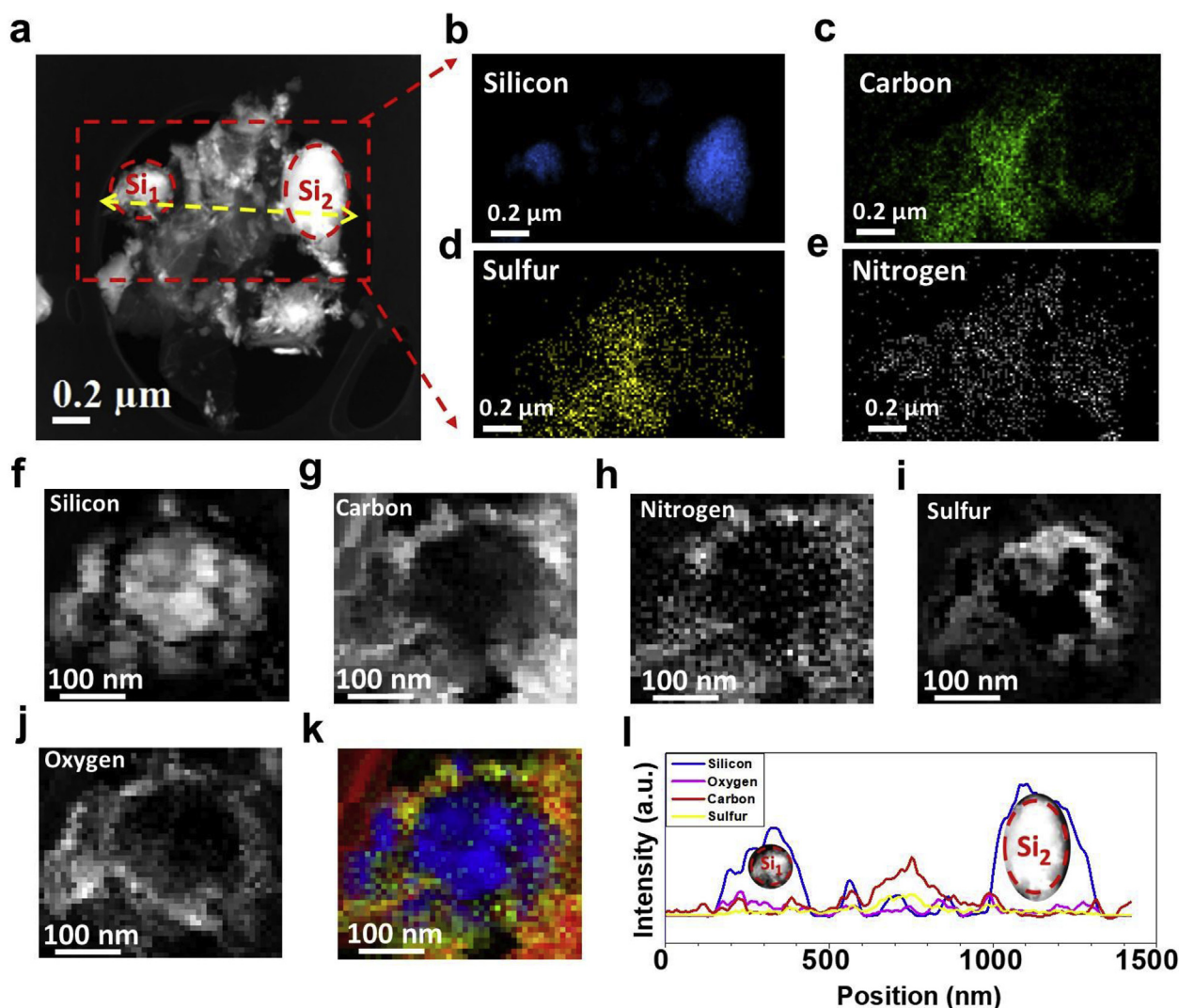


**Fig. 3.** (a) HAADF-STEM image of SG-SiMPs-cPAN composite, (b–e) the EDS mapping of the selected area for silicon, carbon, sulfur, and nitrogen, (f–j) the EELS mapping of the region Si<sub>1</sub>, (k) superimposed EELS color map of silicon (blue), carbon (red), nitrogen (green), (l) EELS line scan (yellow arrow in (a)) across two SG-SiMPs-cPAN particles. (For interpretation of the references to colour in this figure legend, the reader is referred to the Web version of this article.)

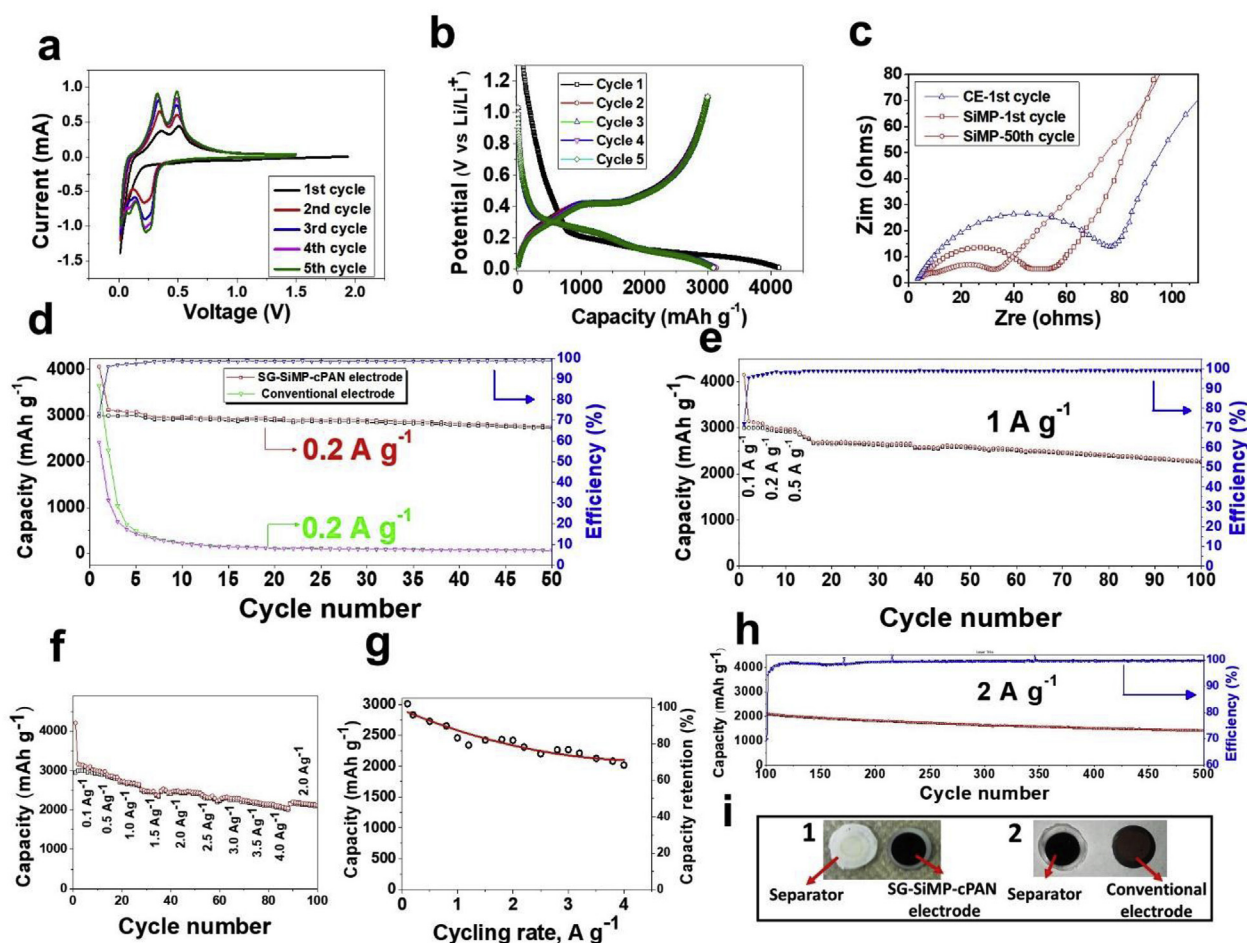
electrodes are summarized in Fig. 4. Cyclic voltammetry (CV) was used to study the lithiation/delithiation behavior of electrodes as shown in Fig. 4a. During the first cathodic scan lithiation of silicon occurs, and only one cathodic peak was observed around  $\sim 0$  V. This peak is associated with the conversion of crystalline silicon to amorphous-silicon (aSi) while forming lithiated-silicon ( $\alpha$ Li-Si). In the anodic portion of the CV curve, delithiation occurs at two stages resulting in the formation of two anodic peaks around 0.32 and 0.50 V. These peaks are attributed to the conversion of  $\alpha$ Li-Si to  $\alpha$ Si. In the subsequent cathodic scans, two more cathodic peaks were observed around 0.27 and 0.22 V due to the transition of  $\alpha$ Si to Li<sub>12</sub>Si<sub>7</sub> and Li<sub>15</sub>Si<sub>4</sub> phases, respectively [41]. The peaks become progressively stronger and broader with cycling due to the activation of material by converting more crystalline silicon into amorphous silicon [26].

Fig. 4b demonstrates the galvanostatic voltage profile of the SG-SiMPs-cPAN electrodes tested at  $0.1 \text{ A g}^{-1}$  between 0.01 and 1.1 V. The discharge profile slightly varies after the first cycle from a typical long plateau to a curve with a gentle slope, which is attributed to the transformation of crystalline silicon into amorphous silicon in subsequent cycles. The first cycle specific discharge capacity of the SG-SiMPs-cPAN electrode is  $4125 \text{ mAh g}^{-1}$  with a coulombic efficiency of 72.5%. The relatively low coulombic efficiency can be attributed to

irreversible lithiation along with SEI formation. However, the coulombic efficiency increased to over 98% within 5 cycles.

Electrochemical impedance spectroscopy (EIS) was conducted to monitor the change of resistance of the electrodes. Fig. 4c shows the Nyquist plot of the SG-SiMPs-cPAN electrode and a conventional electrode composed of SiMPs (60 wt%), Super P (20 wt%) and PVDF (20 wt%). Each plot consists of a semi-circle and a tail. The X-axis intercept at high frequency corresponds to the combined resistance ( $R_s$ ) of the electrolyte, electrode and current collector; whereas the semi-circle diameter represents the combined resistance of charge-transfer ( $R_{CT}$ ) and SEI ( $R_{SEI}$ ). The Nyquist plot shows that the charge transfer resistance of the SG-SiMPs-cPAN electrode is lower than that of the conventional electrode, implying improved electrical connectivity and conductivity of the SG-SiMPs-cPAN electrode. This is reasonable since the PVDF binder of the conventional electrode is electronically insulating, whereas cPAN (after thermolysis) forms an electrically conductive network within the electrode. Thus, cPAN acts both as a binder for mechanical integrity of the electrode, and as a conductive agent to facilitate charge transfer. Furthermore, the decrease in charge transfer resistance after 50 cycles shows the stability of SG-SiMPs-cPAN electrodes during cycling.

The structural stability of the electrodes is evaluated by testing the



**Fig. 4.** (a) Cyclic voltammograms of the SG-SiMPs-cPAN electrode, (b) voltage profile of the SG-SiMPs-cPAN electrode at  $0.1 \text{ A g}^{-1}$ , (c) Nyquist plot of the SG-SiMPs-cPAN and CE electrodes after 1st and 50<sup>th</sup> cycles, (d) cycling stability of the SG-SiMPs-cPAN electrode and conventional electrode at  $0.2 \text{ A g}^{-1}$ , (e) cyclic stability of the SG-SiMPs-cPAN electrode at  $1 \text{ A g}^{-1}$ , (f) rate capability of the SG-SiMPs-cPAN electrode from  $0.1 \text{ A g}^{-1}$  to  $4 \text{ A g}^{-1}$ , (g) capacity retention and specific capacity of the SG-SiMPs-cPAN electrode as a function of cycling rate, (h) cycling stability of cell “f” from 100<sup>th</sup> cycle to 500 cycles at  $2 \text{ A g}^{-1}$ , (i) pictures of the SG-SiMPs-cPAN electrode and conventional electrode after cycling and corresponding separators.

cells under various cycling rates. Fig. 4d shows the cycling stability of the SG-SiMPs-cPAN electrode at  $0.2 \text{ A g}^{-1}$ . The initial discharge capacity of the electrodes is stabilized around  $3000 \text{ mAh g}^{-1}$  at a rate of  $0.1 \text{ A g}^{-1}$  within 5 cycles. Increasing the charging rate to  $0.2 \text{ A g}^{-1}$ , the capacity was  $2730 \text{ mAh g}^{-1}$  after 50 cycles. The SG-SiMPs-cPAN electrode preserved 91% of its initial capacity, which may be attributed to the stability of the SEI on the negative electrode. This reveals that the electrode architecture can buffer the volume change and significantly alleviate electrolyte decomposition. This is mainly due to the robust carbon matrix of cPAN and SG sheets wrapping the silicon particles. For comparison, the conventional electrode was also tested under the same conditions, with its cycling stability shown in Fig. 4d. The discharge capacity decayed significantly after each cycle, very little capacity remaining after only 10 cycles. Upon disassembling the CE cell after testing, it was realized that battery failure resulted from electrode disintegration. This is likely because of the lower binding efficiency of PVDF, which upon charging/discharging led to active material rupture from the copper current collector and catastrophic performance loss (Figs. 4i–2). This highlights the superior electrode structure of SG-SiMPs-cPAN compared to the conventional electrode. To better evaluate the electrochemical performance of SG-SiMPs-cPAN electrodes, faster cycling rates were also applied. Fig. 4e shows the cycling stability of SG-SiMPs-cPAN electrode at  $1 \text{ A g}^{-1}$  which also displays good cycling stability and a discharge capacity of  $2256 \text{ mAh g}^{-1}$  after 100 cycles. Fig. 4f–g shows the rate capability of the SG-SiMPs-cPAN

electrode. The capacity gradually decreased with an increase of cycling rate. Even at  $4 \text{ A g}^{-1}$  current density, a capacity of higher than  $2000 \text{ mAh g}^{-1}$  is retained with a 70% capacity retention (Fig. 4g). Moreover, stable cycling performance was attained when the rate was switched back to  $2 \text{ A g}^{-1}$ , as shown in Fig. 4h. After 500 cycles, the cell has a discharge capacity higher than  $1400 \text{ mAh g}^{-1}$ . This implies that the electrode integrity is preserved without disintegration even at high rates, despite the fact that the silicon particles undergo rapid volume changes during cycling. To further confirm the structural integrity of the electrode, the cell was disassembled after cycling for characterization. The inset of Figs. 4i–1 shows that the electrode material of SG-SiMPs-cPAN is not ruptured from the copper foil after 500 cycles. On the contrary, the CE electrode materials are peeled away from the copper current collector and remain attached to the separator (Figs. 4i–2). This further verifies that the silicon anodes prepared with conventional methods do not possess the desired electrode integrity.

A deeper study on the electrode surface was essential to elucidate the mechanism underlying the improved cycling efficiency. Atomic force microscopy (AFM), SEM and TEM were used to study the surface properties of the electrodes before and after cycling. Before thermolysis, the electrodes had a relatively smooth, continuous surface as shown in Fig. 5a–d. On the contrary, Fig. 5b and 5e–f clearly show that non-continuous micro-channels were formed at the SG-SiMPs-cPAN electrode surface after thermolysis due to the internal stress created with the shrinkage of PAN upon cyclization. Furthermore, following long

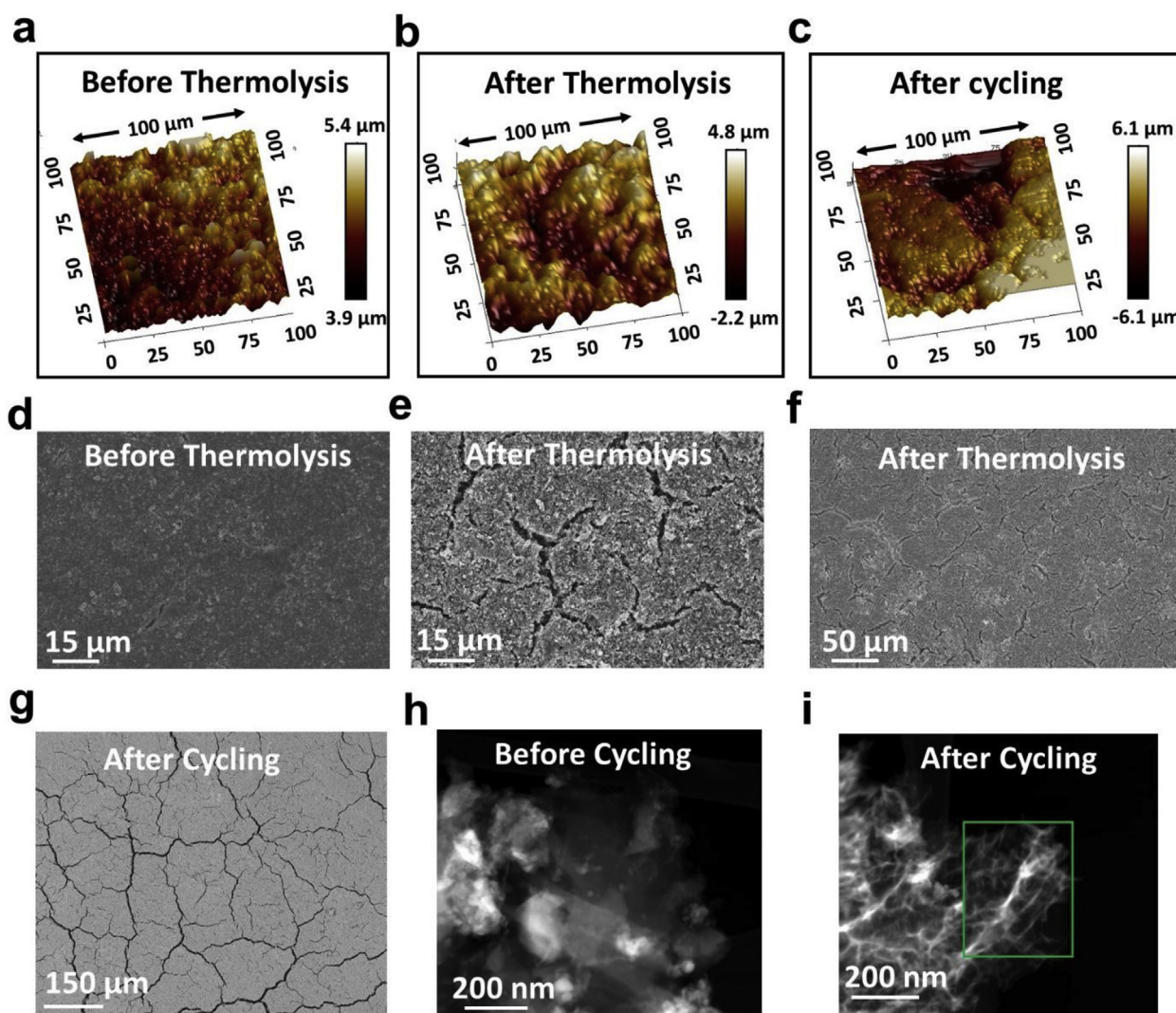


**Fig. 5.** (a) AFM image of the SG-SiMPs-PAN electrode surface before thermolysis, (b) AFM image of the SG-SiMPs-cPAN electrode surface after thermolysis, (c) AFM image of the SG-SiMPs-cPAN electrode surface after cycling, (d) SEM image of the SG-SiMPs-PAN electrode surface before thermolysis, (e) SEM image of the SG-SiMPs-cPAN electrode surface after thermolysis, (f) SEM image of the SG-SiMPs-cPAN electrode after thermolysis, (g) SEM image of the SG-SiMPs-cPAN electrode after cycling (back scattering imaging mode), (h) HAADF-STEM image of the SG-SiMPs-cPAN electrode before cycling, (i) HAADF-STEM image of the SG-SiMPs-cPAN electrode after cycling.

cycling periods, Fig. 5c–g shows the formation of continuous microchannels resembling mudcracking. A similar phenomenon was also observed by Dahn et al. in a study of silicon films [5]. We speculate that this morphology arises in a mode similar to mudcrack formation, whereby the delithiation process of the electrode is analogous to dehydration of mud, resulting in shrinking of silicon particles and crack propagation due to stress fracture. We hypothesize that the void volumes between the electrode “islands” can help to buffer the isotropic silicon volumetric changes during cycling, preventing electrode material rupture and leading to electrode level integrity and good cycling stability. In addition, TEM images (Fig. 5h–i) and corresponding coloured EELS mapping (Figure S5) for the electrode materials show that the silicon particles (bright regions) were distributed evenly and sandwiched between the sheets of NG and SG sheets after cycling, preventing the silicon particle isolation from the carbon matrix. This keeps the integrity at the particle level. Thus, the synergistic effect preserving integrity at the particle and electrode level lead to good cycling stability.

#### 4. Conclusion

In summary, we have fabricated a stable silicon-based anode using commercial SiMPs by developing a two-step top-down approach. Applying a fluid induced fracture (FIF) concept to SiMPs by milling them within an electrode precursor slurry allowed for nanostructuring of the silicon by a straightforward, scalable process. After casting the electrode precursor slurry on the current collector, a thermolysis was applied to achieve an ideally tuned SG-SiMPs-cPAN electrode structure. In this structure, the polymer binder (PAN) was converted into a 3D conductive network of cPAN that wrapped the silicon particles and demonstrated the formation of micron sized channels throughout the electrode structure. These void micro-channels acted as a mechanical buffer for the anisotropic volume changes of silicon particles during battery charging/discharging, thereby preventing electrode pulverization. This electrode structure provides excellent capacity ( $3081 \text{ mAh g}^{-1}$  @  $0.1 \text{ A g}^{-1}$ ) in addition to good rate capabilities and cycle life ( $1423 \text{ mAh g}^{-1}$  @  $2 \text{ A g}^{-1}$  for 500 cycles). Furthermore, the efficiency of this technique makes it possible to expand its application to other anode materials that require mechanical robustness and electrical conductivity with the goal of preparing next generation lithium-ion

batteries.

## Acknowledgements

We would like to acknowledge financial support from the Natural Sciences and Engineering Research Council of Canada (NSERC), the University of Waterloo, and the Waterloo Institute for Nanotechnology. TEM and HAADF–STEM were obtained at the Canadian Center for Electron Microscopy (CCEM) located at McMaster University.

## Appendix A. Supplementary data

Supplementary data related to this article can be found at <https://doi.org/10.1016/j.jpowsour.2018.08.035>.

## References

- [1] M.T. McDowell, S.W. Lee, W.D. Nix, Y. Cui, *Adv. Mater.* 25 (36) (2013) 4966–4985.
- [2] F.M. Hassan, A.R. Elsayed, V. Chabot, R. Batmaz, X. Xiao, Z. Chen, *ACS Appl. Mater. Interfaces* 6 (16) (2014) 13757–13764.
- [3] H. Wu, Y. Cui, *Nano Today* 7 (5) (2012) 414–429.
- [4] T. Hatchard, J. Dahn, *J. Electrochem. Soc.* 151 (6) (2004) A838–A842.
- [5] L.Y. Beaulieu, K.W. Eberman, R.L. Turner, L.J. Krause, J.R. Dahn, *Electrochem. Solid state Lett.* 4 (9) (2001) A137–A140.
- [6] H. Wu, G. Chan, J.W. Choi, Y. Yao, M.T. McDowell, S.W. Lee, A. Jackson, Y. Yang, L. Hu, Y. Cui, *Nat. Nanotechnol.* 7 (5) (2012) 310–315.
- [7] C.K. Chan, H.L. Peng, G. Liu, K. McIlwrath, X.F. Zhang, R.A. Huggins, Y. Cui, *Nat. Nanotechnol.* 3 (1) (2008) 31–35.
- [8] I. Kovalenko, B. Zdyrko, A. Magasinski, B. Hertzberg, Z. Milicev, R. Burtovyy, I. Luzinov, G. Yushin, *Science* 334 (6052) (2011) 75–79.
- [9] A. Magasinski, P. Dixon, B. Hertzberg, A. Kvit, J. Ayala, G. Yushin, *Nat. Mater.* 9 (5) (2010) 461–461.
- [10] F.M. Hassan, R. Batmaz, J. Li, X. Wang, X. Xiao, A. Yu, Z. Chen, *Nat. Commun.* 6 (2015).
- [11] N. Liu, Z.D. Lu, J. Zhao, M.T. McDowell, H.W. Lee, W.T. Zhao, Y. Cui, *Nat. Nanotechnol.* 9 (3) (2014) 187–192.
- [12] H. Wu, G. Yu, L. Pan, N. Liu, M.T. McDowell, Z. Bao, Y. Cui, *Nat. Commun.* 4 (2013) 1943.
- [13] L.-F. Cui, R. Ruffo, C.K. Chan, H. Peng, Y. Cui, *Nano Lett.* 9 (1) (2008) 491–495.
- [14] X.H. Liu, L. Zhong, S. Huang, S.X. Mao, T. Zhu, J.Y. Huang, *ACS Nano* 6 (2) (2012) 1522–1531.
- [15] M. Ko, S. Chae, S. Jeong, P. Oh, J. Cho, *ACS Nano* 8 (8) (2014) 8591–8599.
- [16] S. Sim, P. Oh, S. Park, Cho, *J. Adv. Mater.* 25 (32) (2013) 4498–4503.
- [17] U. Kasavajjula, C. Wang, A.J. Appleby, *J. Power Sources* 163 (2) (2007) 1003–1039.
- [18] M. Obrovac, L. Krause, *J. Electrochem. Soc.* 154 (2) (2007) A103–A108.
- [19] J.H. Ryu, J.W. Kim, Y.-E. Sung, S.M. Oh, *Electrochem. Solid state Lett.* 7 (10) (2004) A306–A309.
- [20] R. Yi, F. Dai, M.L. Gordin, S. Chen, D. Wang, *Adv. Energy Mater.* 3 (3) (2013) 295–300.
- [21] B.M. Bang, H. Kim, H.-K. Song, J. Cho, S. Park, *Energy Environ. Sci.* 4 (12) (2011) 5013–5019.
- [22] B.M. Bang, J.I. Lee, H. Kim, J. Cho, S. Park, *Adv. Energy Mater.* 2 (7) (2012) 878–883.
- [23] Y. Li, K. Yan, H.-W. Lee, Z. Lu, N. Liu, Y. Cui, *Nat. Energy* 1 (2016) 15029.
- [24] I.-S. Kim, P.N. Kumta, *J. Power Sources* 136 (1) (2004) 145–149.
- [25] G. Wang, J. Yao, H. Liu, *Electrochem. Solid state Lett.* 7 (8) (2004) A250–A253.
- [26] X. Chen, X. Li, F. Ding, W. Xu, J. Xiao, Y. Cao, P. Meduri, J. Liu, G.L. Graff, J.-G. Zhang, *Nano Lett.* 12 (8) (2012) 4124–4130.
- [27] C. Wang, G. Wu, X. Zhang, Z. Qi, W. Li, *J. Electrochem. Soc.* 145 (8) (1998) 2751–2758.
- [28] Y. Zhang, X. Zhang, H. Zhang, Z. Zhao, F. Li, C. Liu, H. Cheng, *Electrochim. Acta* 51 (23) (2006) 4994–5000.
- [29] Y. Sun, N. Liu, Y. Cui, *Nat. Energy* 1 (2016) 16071.
- [30] D.C. Marcano, D.V. Kosynkin, J.M. Berlin, A. Sinititskii, Z. Sun, A. Slesarev, L.B. Alemany, W. Lu, J.M. Tour, *ACS Nano* 4 (8) (2010) 4806–4814.
- [31] G. Holland, B.S. Lollar, L. Li, G. Lacrampe-Couloume, G. Slater, C. Ballentine, *Nature* 497 (7449) (2013) 357–360.
- [32] M.H. Anders, S.E. Laubach, C.H. Scholz, *J. Struct. Geol.* 69 (2014) 377–394.
- [33] S. Stanchits, S. Mayr, S. Shapiro, G. Dresen, *Tectonophysics* 503 (1) (2011) 129–145.
- [34] M.S.A. Rahaman, A.F. Ismail, A. Mustafa, *Polym. Degrad. Stabil.* 92 (8) (2007) 1421–1432.
- [35] Q. Ouyang, L. Cheng, H. Wang, K. Li, *Polym. Degrad. Stabil.* 93 (8) (2008) 1415–1421.
- [36] S. Arbab, A. Zeinolebadi, *Polym. Degrad. Stabil.* 98 (12) (2013) 2537–2545.
- [37] T.J. Xue, M.A. McKinney, C.A. Wilkie, *Polym. Degrad. Stabil.* 58 (1) (1997) 193–202.
- [38] G. Scardera, T. Puzzer, G. Conibeer, M. Green, *J. Appl. Phys.* 104 (10) (2008) 104310.
- [39] S.-A. Wohlgemuth, F. Vilela, M.-M. Titirici, M. Antonietti, *Green Chem.* 14 (3) (2012) 741–749.
- [40] R. Jansen, H. Van Bekkum, *Carbon* 33 (8) (1995) 1021–1027.
- [41] B. Liu, P. Soares, C. Checkles, Y. Zhao, G. Yu, *Nano Lett.* 13 (7) (2013) 3414–3419.